

Rapid Image Evaluation System for Corneal In Vivo Confocal Microscopy

Christine W. Sindt, OD,* Bruno Lay, PhD,† Helene Bouchard,‡ and Jami R. Kern, PhD‡

Purpose: To develop rapid image processing techniques for the objective analysis of corneal in vivo confocal micrographs.

Methods: Perpendicular central corneal volume scans from healthy volunteers were obtained via laser in vivo confocal microscopy. The layer in each volume scan that contained the nerve plexus was detected by applying software operators to analyze image features on the basis of their size, shape, and contrast. Dendritic immune cells were detected in the nerve image on the basis of cellular size, lack of elongation, and brightness relative to the nerves. Images that were 20 μm anterior to the best nerve layer images were used for the analysis of epithelial wing cells; wing cell detection was based on extended regional minima and a watershed transformation.

Results: The software successfully detected the best nerve layer images in 15 scans from 15 eyes. Manual and automatic analyses were 81.8% in agreement for dendritic immune cells (for 11 cells in a representative image) and 94.4% in agreement for wing cells (for 466 cells in the image). Within 10 seconds per scan, the software calculated the number, mean length, and mean density of immune cells; the number, mean size, and mean density of wing cells; and the number and mean length of nerves. Factors defining the shape and position of cells and nerves also were available.

Conclusions: The software rapidly and accurately analyzed the in vivo confocal micrographs of the healthy central corneas, yielding quantitative results to describe the nerves, dendritic immune cells, and wing cells.

Key Words: in vivo confocal microscopy, cornea, nerve, wing cell, dendritic immune cell, image processing, image analysis

(*Cornea* 2012;0:1–6)

Received for publication December 1, 2011; revision received April 9, 2012; accepted April 14, 2012.

From the *Department of Ophthalmology, University of Iowa, Iowa City, IA; †ADCIS, Saint-Contest, France; and ‡Alcon Research Ltd, Fort Worth, TX.

Alcon funded this research and provided the services of a medical writer to assist with the preparation of this manuscript. A patent that resulted from this study names CWS, BL, and JRK as inventors.

The authors have no conflicts of interest to disclose.

Supplemental digital content is available for this article. Direct URL citations appear in the printed text and are provided in the HTML and PDF versions of this article on the journal's Web site (www.corneajrnl.com).

Reprints: Christine W. Sindt, Contact Lens Service, Department of Ophthalmology & Visual Science, University of Iowa, 200 Hawkins Dr, Iowa City, IA 52242-1091 (e-mail: christine-sindt@uiowa.edu).

Copyright © 2012 by Lippincott Williams & Wilkins

In vivo confocal microscopy of the cornea has been used to characterize conditions such as infectious keratitis (in particular, *Acanthamoeba* keratitis¹ and fungal keratitis^{2,3}); corneal dystrophies⁴; contact lens wear⁵; diabetic neuropathy⁶; and other states of corneal disease, disorder, and health. Recent reviews of corneal in vivo confocal microscopy have summarized the upswing of this technology.^{7–11}

The massive amount of data yielded by corneal in vivo confocal microscopy is difficult to analyze and interpret with consistency and efficiency. Therefore, quantitative applications of this technology have required time-consuming analysis. For example, the variety of layers in the epithelium makes it difficult for researchers to identify the same layer consistently between patients or between time points. Attempts to quantify basal epithelial wing cells yielded high variability between types of confocal microscopes and between studies.⁷ Quantifying epithelial wing cells required researchers to manually look for landmarks while adjusting the microscope in the z-direction during image collection and then to manually count the cells during image analysis.¹²

The nerve layer may serve as a better landmark than any epithelial layer, but analyses of nerves required some early research to establish a scheme to process the images to quantify the number and density of nerves in an image frame and to quantify the diameter, tortuosity, beading, and reflectivity of each nerve.¹³ Several other researchers^{14–17} followed this earlier manual analysis scheme in whole or in part. Dendritic immune cells may occur in the same layer as the nerve layer, but analysis of these cells required researchers to manually identify and tag the cells in the software for quantitative analysis.^{5,18,19}

Software solutions have recently made corneal in vivo confocal microscopy more convenient. Software for analyses of nerves include a nerve-mapping module that can build a composite image after an analyst manually follows the paths of nerves in the x and y directions²⁰ and a semi-automated tracing program for length, branching, and number (although tortuosity was still graded manually).²¹ Software for analyses of dendritic cells include a cell-counting plug-in module (which still required a manual mode) and a separate image analysis program that was capable of measuring cell area and number of dendrites per cell.²¹

This project was designed to develop robust and rapid image processing techniques that could integrate together in one software and suite the objective analysis of corneal nerves, wing cells, and dendritic cells.

MATERIALS AND METHODS

Image Sources

Images were obtained bilaterally from 48 healthy volunteers who had provided informed consent to participate in a related clinical trial that was registered at ClinicalTrials.gov as NCT00804999. Subjects met a list of prespecified ocular health criteria as previously described^{22,23} and were habitual wearers of soft contact lenses ($n = 38$) or were naive to contact lens wear ($n = 10$). The 15 best representative scans were selected from this data set.

Confocal Microscopy

A central corneal scan was taken with a Heidelberg Retina Tomograph Rostock Cornea Module (Heidelberg Engineering GmbH, Heidelberg, Germany). The light source was a 670-nm diode laser (class 1) with a theoretical 1- μm resolution. Images were captured with an area of $400 \times 400 \mu\text{m}^2$ and a digital image size of 384×384 pixels (for a total of 147,456 pixels); because pixel sizes were larger than 1 μm , the resolution was limited by the pixels. Each volume scan captured a series of 40 images from the epithelium to the anterior stroma, in 2- μm increments, yielding an 80- μm stack of images (as opposed to the other modes of the microscope, which yield sequence scans or still images). The ophthalmic photographer captured at least 4 volume scans per eye; extra scans were captured if alignment problems were encountered or suspected. Volume scans that were oblique tended to have cell definition that varied in the x/y directions, as shown in **Supplemental Digital Content 1** (see **Figure**, <http://links.lww.com/ICO/A69>); these scans were discarded from the database.

Software Development

Identification of the Best Nerve Layer Image

The software was designed to detect first, in each image stack from a volume scan, the layer that contained most of the nerve plexus. Nerves in the confocal images appeared as white objects (on a dark background) with an elongated and thinned shape. Therefore, image processing operators (as described in **Supplemental Digital Content 2**, <http://links.lww.com/ICO/A70>) were designed to automatically detect the layer that contained such bright and thin objects. The resultant identified layer was called the best nerve layer image.

After determination of the best nerve layer image, the software prompted the user to validate the result. If the user did not agree with the automatically detected best nerve layer image, the software allowed the user to select a different image in the series that could become the best nerve layer image. Consequently, the newly selected image would be used to set the parameters for the detection of immune and wing cells.

Analysis of Nerves

The functions described in **Supplemental Digital Content 2** (<http://links.lww.com/ICO/A70>) were sufficient to detect the layer that contained the best nerve image but were not optimal for analyzing the nerves within that image.

The functions described below were designed to provide optimal nerve detection within the best nerve layer image. First, an opening transformation based on a square of size 11×11 pixels was applied, and the opened image was subtracted from the original image to compensate for the unevenness of the background (Fig. 1B). Then, a hysteresis threshold²⁴ was applied to generate a binary image. The hysteresis threshold used both an upper and a lower threshold. A subset of the nerve plexus was detected by the upper threshold, but with missing components; the upper threshold was then reconstructed in the lower threshold (Figs. 1C–E). The hysteresis threshold helped to detect only the relevant objects in an image, removing the small artifacts when images were noisy or when nerves had nonuniform intensity. Finally, a closing transformation based on a disk with a diameter of 7 pixels was applied to the binary image to reconnect the nerves (Fig. 1F).

After the transformations were applied, the software computed a skeleton, detected branching points on that skeleton, and analyzed each branch. Analysis of the minimum bounding box surrounding each terminal branch of the skeleton included the measurement of the angle of the box relative to the main direction of the neighboring branch of the skeleton and the elongation ratio of each branch.

After automatic detection of nerves, the postprocessing mode of the software could be used to make further manipulations of nerve analysis. These manipulations included drawing lines to highlight nerves that had been missed during automatic recognition, deleting lines that represented features (such as immune cells) that had been mistakenly identified as nerves, and connecting lines that represented 2 parts of the same nerve that had not been properly connected during image processing.

Analysis of Dendritic Immune Cells

The dendritic immune cells were detected and analyzed in the best nerve layer image. Dendritic immune cells appeared in the images as small, white, and usually compact objects, as shown in Figures 1A and G. These cells could occur anywhere in the best nerve layer image: either isolated from the nerves or connected to the nerves (appearing as small branches on the nerve network). To analyze these dendritic immune cells, the nerves in the same image had to be excluded from the analysis. The algorithms to detect dendritic immune cells involved the operators described in **Supplemental Digital Content 3** (<http://links.lww.com/ICO/A71>).

The software was designed to allow the user to manually enhance the automatic detection of the immune cells in a postprocessing step, in case the detection process was suboptimal. After detection of immune cells, the postprocessing mode could be used to manually mark cells that had been missed by the automatic detection or to delete features that had been mistakenly recognized as immune cells by the automatic detection.

Analysis of Wing Cells

The wing cells were detected and analyzed in the image that was 20 μm anterior (10 image layers anterior) to the best nerve layer image. The value of 20 μm was determined by manual analysis of a set of 10 scans; during this analysis, layers of wing cells were usually observed starting at 10 μm (5 image

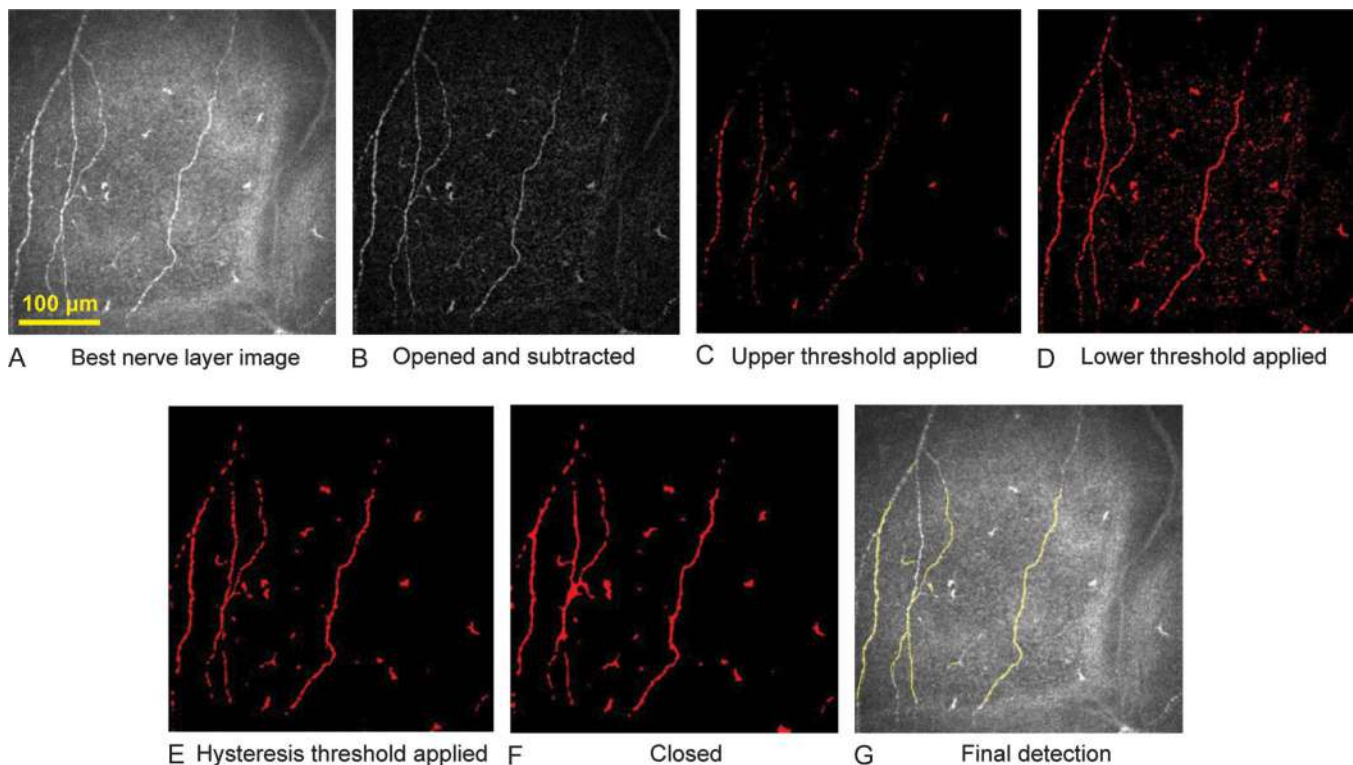


FIGURE 1. A–G, Steps for automatic detection of the nerve plexus in the best nerve layer image. The untransformed image (panel A) was at layer 22 of 40 layers in the volume scan.

layers) anterior to the best nerve layer image and extending through 30 μm (15 image layers) anterior to the best nerve layer image. The center of that thickness was targeted for wing cell analysis because that center layer provided good cell definition and allowed some flexibility (ie, missing the targeted center of the layer was still likely to yield a wing cell layer near the center, whereas missing a targeted edge layer could yield an image layer outside of the wing cell layers).

Wing epithelial cells (in the center of the epithelium) were targeted for analyses rather than basal epithelial cells (most posterior in epithelium) or superficial epithelial cells (most anterior in epithelium), for a number of reasons. Basal epithelial cells may present the following problems in analyses: indistinct cell borders in confocal micrographs, with borders becoming more pronounced in corneas with edema²⁵; cellular density that is relatively consistent among some types of corneal disorders,²⁵ making this layer an unreliable marker of corneal health; and a density that seems to vary between types of confocal microscopes and between studies.⁷ Superficial epithelial cells may be a sensitive measure of corneal health but may be altered by the contact nature of *in vivo* confocal microscopy or its associated application of corneal anesthetic,⁷ making superficial cells unsuitable for repeated analyses. For these reasons, wing cells were chosen for analysis: these cells were expected to have a potential to reflect corneal health, to be consistent between measurements, and to be detected relatively easily (because of bright cell borders) in automated analysis.

See Figure 2A for an example image of a wing cell layer. The first step of wing cell detection was a closing

transformation based on a disk with a diameter of 3 pixels that was applied to connect any wing cell boundaries that were not perfectly uniform. This operation helped to generate a bright boundary splitting each cell from its neighbors. Then, extended regional minima were detected; these were the darker centers of cells (with lower values, nearer to 0 = black) within the brighter cell boundaries (with higher values, nearer to 255 = white). Extended regional minima had a tolerance of 15 units to smooth the neighboring minima and to reduce the noise effect (Fig. 2B). Thereafter, a watershed transformation²⁶ was applied, using the regional minima as seed markers, to generate the boundaries between neighboring regional minima (Fig. 2C). A boundary detection was derived from the watershed.

All cells that intersected the edges of the frame of the image were removed from the processing to avoid biasing the results with poorly illuminated or poorly defined cells and to highlight the well-defined cells in the center of the image, as shown in Figure 2D. The outer boundary of a group of all detected wing cells defined a region of interest that was available for later use in manual annotations. The software was designed to allow the user to manually change some of the parameters to enhance the detection of wing cells, in case the detection process was suboptimal; see **Supplemental Digital Content 4** (see Figure, <http://links.lww.com/ICO/A72>).

Tabulation of Nerve and Cell Data

After all detection parameters were calculated (with or without manual enhancements), the software computed

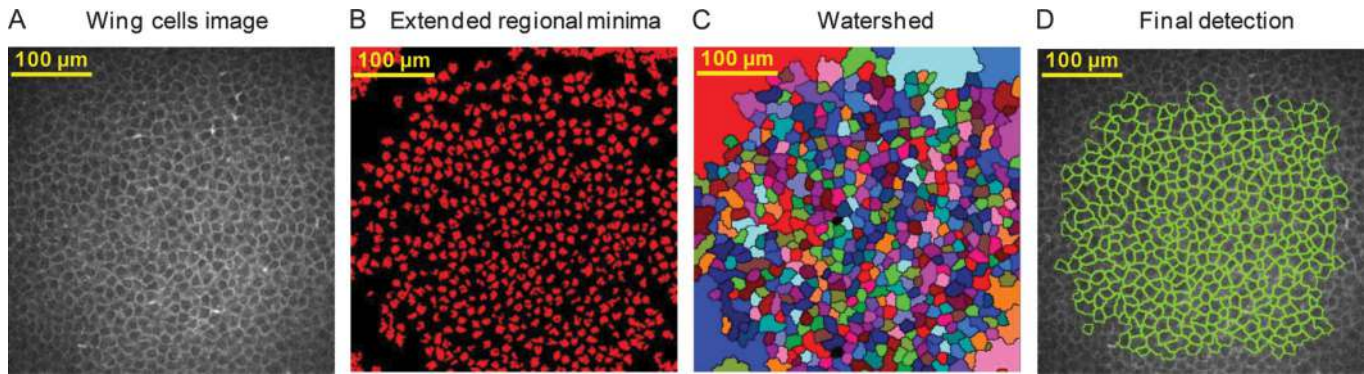


FIGURE 2. A–D, Detection of wing cells in the same volume scan of the same eye as shown in Figure 1.

measurements for the nerves, the wing cells, and the immune cells. The standard measurements included the following: image layers (from layer 1 to layer 40, in a 40-image depth stack from a volume scan) for nerves, immune cells, and wing cells; numbers of nerves, immune cells, and wing cells; average surface areas of wing cells and immune cells; densities of immune cells and wing cells (number of cells divided by the sum of the surface area of the cells); and average lengths of immune cells and nerves. The measurements were designed to be exportable as a summary table that would be compatible with standard spreadsheet software.

More details about wing cells and immune cells also could be obtained from the software. Additional measurements were available as a grid and included per-cell surface area, perimeter, compactness, and circularity. These per-cell measurements were calculated in calibrated units that were consistent within the software. The results were designed to be easily exportable for statistical analysis outside of the software or could be plotted as a histogram within the software.

Validation: Manual Versus Automatic Results

A validation menu was designed to allow the user to compare manual analysis results with automatic analysis results. The region of interest defined during the wing cell detection was presented to the user, who could use a mouse to click inside each wing cell and immune cell (in their respective layers) to mark them for counting. After manual marking, a summary table of manual annotation was generated and was compared with the automatic annotation results. The validation results were designed to be easily exportable to standard spreadsheet software.

RESULTS

Overall/Population-Level Results

The software that was developed in this study was named ARIES 2D, which stands for AIConfocal Rapid Image Evaluation System, 2-dimensional version (Alcon Research Ltd, Fort Worth, TX). The software successfully detected the best nerve layer images in 15 perpendicular volume scans from 15 eyes within 10 seconds each, without returning any erroneously identified layers, as confirmed by manual

quality check by the investigators. Sample results for an individual eye are shown in **Supplemental Digital Content 5** (<http://links.lww.com/ICO/A73>).

Sample Results for Nerves

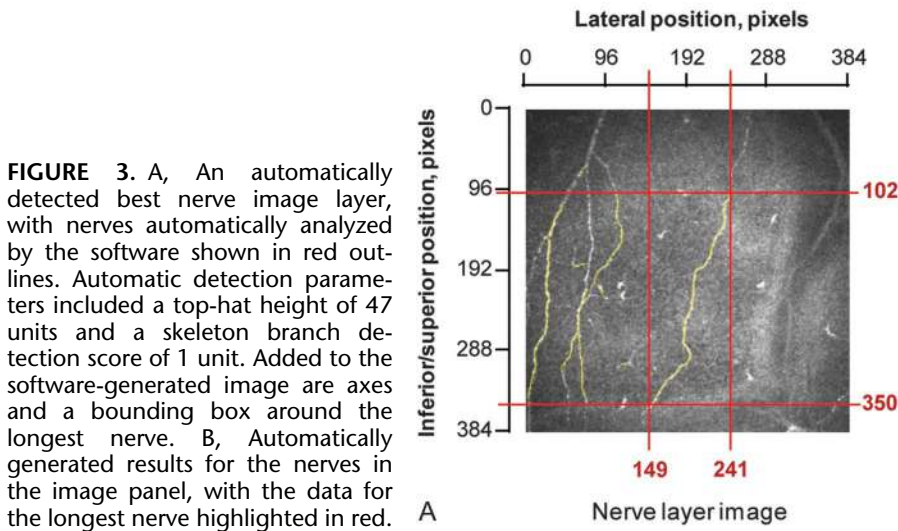
Sample results for an automatic analysis (without manual enhancement) of a nerve plexus, including position and length of each nerve, are shown in Figure 3. The nerve plexus for this sample was identified in image layer 22 (of 40 image layers). This nerve plexus contained 11 nerves that had an average length within the image of 83 μm .

Sample Results for Immune Cells

Figure 4A shows an example of an image wherein the software automatically detected the best nerve layer image and then drew outlines around the immune cells in that layer. Figure 4B shows the resultant software-generated calculations for the surface area of individual cells, the coordinates of the rectangles bounding each cell, the number of pixels defining each cell, and the width of each cell. As shown in **Supplemental Digital Content 5** (<http://links.lww.com/ICO/A73>) the immune cells were analyzed in image layer 22 (the same layer as the best nerve layer image). This image contained 12 immune cells, with each cell having an average length of 9.9 μm and an average density of 0.024 cells per square micrometer. The inverse of that cell density (1/0.024) indicated the average cell area: 42 μm^2 .

Sample Results for Wing Cells

As shown in **Supplemental Digital Content 5** (<http://links.lww.com/ICO/A73>) the wing cells were analyzed in image layer 12 (or 10 layers anterior to the best nerve layer image in layer 22). The region of interest in this image contained 408 wing cells, with each cell having an average size of 176 μm^2 (and inversely, with each cell having an average density of 0.00569 cells per square micrometer). The software calculated characteristics for each of the 408 cells in **Supplemental Digital Content 6** (see **Figure**, <http://links.lww.com/ICO/A74>); for simplicity, results for only one cell are described there.



Keys	Bounding Box (x ₁ ; y ₁ ; x ₂ ; y ₂)	Length, μm
1	(64; 67; 71; 76)	10.5
2	(149; 102; 241; 350)	300.0
3	(70; 103; 115; 211)	121.6
4	(0; 112; 43; 343)	253.8
5	(55; 181; 72; 187)	20.5
6	(77; 209; 80; 211)	2.4
7	(84; 209; 91; 220)	13.1
8	(63; 213; 74; 237)	27.1
9	(61; 241; 72; 345)	107.6
10	(42; 271; 60; 314)	50.6
11	(112; 302; 120; 304)	7.4

Manual Versus Automatic Validation

As shown in **Supplemental Digital Content 7** (see **Figure**, <http://links.lww.com/ICO/A75>), the validation summary table indicated acceptable agreement between the manual and automatic counting of immune cells and wing cells. Both the user and the software counted 11 features as immune cells, although the user and software did not count the same 11 features as immune cells in all cases: 9 of 11 features (81.8%) were identified as immune cells by both the software and the user. The investigator counted 473 wing cells and the software counted 466 wing cells. The ideal value for wing cells detected and marked is 100%; the actual value was 94.4% (of the 466 cells that were automatically detected, 440 of them were both marked by the user and detected by the software).

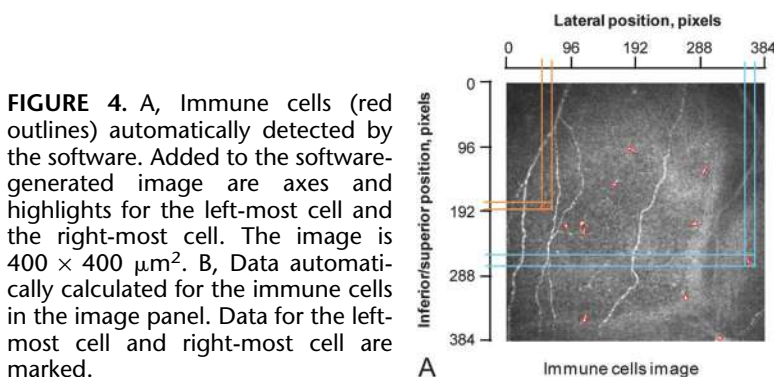
DISCUSSION

The software that was developed in this study was used to successfully analyze perpendicular volume scans from laser in vivo confocal microscopy of the central corneas of healthy volunteers. Analyses were rapid (<10 seconds), consistent (best nerve layer image correctly identified in 15 scans from 15 eyes), and accurate (>81.8% agreement with manual analyses in a representative sample) and yielded

unprecedented levels of automated quantitative information about corneal microstructures (including shapes, sizes, and densities of nerves, wing cells, and dendritic immune cells).

This software is expected to be a valuable addition to existing software that has been developed for the analysis of nerves^{20,21} and dendritic cells²¹ and should fill a gap for the software-based analysis of epithelial cells (specifically, wing cells of the epithelium). Moreover, this software is expected to be a large improvement on the manual analysis of in vivo confocal micrographs that is standard for most studies.

Although the software seemed to successfully meet the planned objectives, this study did have a number of limitations. The software was developed from, and was tested on, only images from a single set of healthy eyes of soft contact lens wearers or those who were naive to contact lens wear; future studies should apply the software to various diseases and disorders. Verification is needed from larger populations to demonstrate the ability of the software to discriminate between levels of corneal health and disease. The software has been tested only with laser in vivo confocal microscopy having 2-μm resolution in the z-direction, not with slit-scanning in vivo confocal microscopy having 4-μm resolution in the z-direction. The software is somewhat dependent on the skill of the technician or photographer in obtaining perpendicular scans. Also, the 2-dimensional



Keys	Area, μm	Bounding Box (x ₁ ; y ₁ ; x ₂ ; y ₂)	Pixel Count	Width, μm
7	47.7	(180; 95; 190; 103)	44	12.8
17	42.3	(291; 125; 297; 135)	39	12.0
25	29.3	(156; 149; 163; 154)	27	7.3
40	29.3	(54; 181; 62; 188)	27	8.3
48	51.0	(109; 205; 116; 213)	47	8.3
49	44.5	(274; 205; 283; 212)	41	10.4
51	35.8	(85; 209; 91; 216)	33	7.3
54	39.1	(113; 216; 118; 226)	36	10.4
73	47.7	(356; 258; 364; 269)	44	13.5
96	44.5	(263; 314; 270; 322)	41	8.3
100	53.2	(113; 343; 119; 355)	49	13.3
104	33.6	(314; 375; 321; 381)	31	7.3

version of the software described in this manuscript did not “register” images to account for saccadic movements that occurred during volume scan acquisition. Registration and reconstruction have been described elsewhere²⁷ and is in development for a forthcoming 3-dimensional application of the software.²⁸ Finally, the manual versus automatic validation indicated room for improvement: For ideal values of 100% agreement, actual values were 81.8% for immune cells and 94.4% for wing cells.

In vivo confocal microscopy is making the transition “from bench to bedside”⁸; this software could be valuable in that process. For example, in vivo confocal microscopy has been used in qualitative forms or in manually quantitative forms for the purposes of characterizing severe corneal states, such as keratitis^{1–3} or graft rejection.^{18,29} The software could make it possible for researchers and physicians to detect subclinical changes during or after these extreme states. For example, a patient who seems to have a quiet white eye after an infection could be checked by software-assisted in vivo confocal microscopy to ensure that the corneal response had truly subsided, even at the subclinical level of dendritic immune cells, before the clinician approves the patient to resume wearing contact lenses. Similarly, with graft survival, the software could be used to guide clinical decisions about dosages of topical steroids, by allowing the clinician to view nerve state and dendritic immune cells in the cornea that were not observable clinically. These applications are speculations, but we look forward to seeing researchers and clinicians investigate the utility of the software for such purposes.

The software also could guide industrial research, so that manufacturers could develop ophthalmic products that minimize subclinical immune responses in the cornea. Corneal responses to contact lenses or lens care products may be less obvious, but more prevalent, than responses to infection or inflammation. Software-assisted in vivo confocal microscopy could reveal subclinical responses to contact lenses or lens care solutions that have been laborious to analyze manually.^{5,22,23}

In summary, the newly developed software was capable of analyzing perpendicular volume scans from laser in vivo confocal microscopy of the central corneas of healthy volunteers, yielding results quickly, consistently, and accurately. This software should be a useful addition to clinical practice and research.

REFERENCES

- Shiraishi A, Uno T, Oka N, et al. In vivo and in vitro laser confocal microscopy to diagnose acanthamoeba keratitis. *Cornea*. 2010;29:861–865.
- Takezawa Y, Shiraishi A, Noda E, et al. Effectiveness of in vivo confocal microscopy in detecting filamentous fungi during clinical course of fungal keratitis. *Cornea*. 2010;29:1346–1352.
- Das S, Samant M, Garg P, et al. Role of confocal microscopy in deep fungal keratitis. *Cornea*. 2009;28:11–13.
- Labbé A, De Nicola R, Dupas B, et al. Epithelial basement membrane dystrophy: evaluation with the HRT II Rostock Cornea Module. *Ophthalmology*. 2006;113:1301–1308.
- Zhivov A, Stave J, Vollmar B, et al. In vivo confocal microscopic evaluation of langerhans cell density and distribution in the corneal epithelium of healthy volunteers and contact lens wearers. *Cornea*. 2007;26:47–54.
- Tavakoli M, Kallinikos P, Iqbal A, et al. Corneal confocal microscopy detects improvement in corneal nerve morphology with an improvement in risk factors for diabetic neuropathy. *Diabet Med*. 2011;28:1261–1267.
- Niederer RL, McGhee CN. Clinical in vivo confocal microscopy of the human cornea in health and disease. *Prog Retin Eye Res*. 2010;29:30–58.
- Guthoff RF, Zhivov A, Stachs O. In vivo confocal microscopy, an inner vision of the cornea—a major review. *Clin Experiment Ophthalmol*. 2009;37:100–117.
- Erie JC, McLaren JW, Patel SV. Confocal microscopy in ophthalmology. *Am J Ophthalmol*. 2009;148:639–646.
- Baudouin C, Labbe A, Dupas B. Imaging the ocular surface with confocal microscopy: histology without samples [in French]. *J Fr Ophthalmol*. 2008;31:308–316.
- Kaufman SC, Musch DC, Belin MW, et al. Confocal microscopy: a report by the American Academy of Ophthalmology. *Ophthalmology*. 2004;111:396–406.
- Eckard A, Stave J, Guthoff RF. In vivo investigations of the corneal epithelium with the confocal Rostock Laser Scanning Microscope (RLSM). *Cornea*. 2006;25:127–131.
- Oliveira-Soto L, Efron N. Morphology of corneal nerves using confocal microscopy. *Cornea*. 2001;20:374–384.
- Villani E, Galimberti D, Viola F, et al. The cornea in Sjogren's syndrome: an in vivo confocal study. *Invest Ophthalmol Vis Sci*. 2007;48:2017–2022.
- Benitez-del-Castillo JM, Acosta MC, Wassfi MA, et al. Relation between corneal innervation with confocal microscopy and corneal sensitivity with noncontact esthesiometry in patients with dry eye. *Invest Ophthalmol Vis Sci*. 2007;48:173–181.
- Benitez-del-Castillo JM, Wasfy MA, Fernandez C, et al. An in vivo confocal masked study on corneal epithelium and subbasal nerves in patients with dry eye. *Invest Ophthalmol Vis Sci*. 2004;45:3030–3035.
- Zhang M, Chen J, Luo L, et al. Altered corneal nerves in aqueous tear deficiency viewed by in vivo confocal microscopy. *Cornea*. 2005;24:818–824.
- Mastropasqua L, Nubile M, Lanzini M, et al. Epithelial dendritic cell distribution in normal and inflamed human cornea: in vivo confocal microscopy study. *Am J Ophthalmol*. 2006;142:736–744.
- Zhivov A, Stave J, Vollmar B, et al. In vivo confocal microscopic evaluation of Langerhans cell density and distribution in the normal human corneal epithelium. *Graefes Arch Clin Exp Ophthalmol*. 2005;243:1056–1061.
- Zhivov A, Blum M, Guthoff R, et al. Real-time mapping of the subepithelial nerve plexus by in vivo confocal laser scanning microscopy. *Br J Ophthalmol*. 2010;94:1133–1135.
- Cruzat A, Witkin D, Baniyadi N, et al. Inflammation and the nervous system: the connection in the cornea in patients with infectious keratitis. *Invest Ophthalmol Vis Sci*. 2011;52:5136–5143.
- Sindt CW, Grout TK, Critser DB, et al. Dendritic immune cell densities in the central cornea associated with soft contact lens types and lens care solution types: a pilot study. *Clin Ophthalmol*. 2012;6:511–519.
- Sindt CW, Critser DB, Grout TK, et al. Effects of fluorescein staining on laser in vivo confocal microscopy images of the cornea. *J Ophthalmol*. 2012;2012:541974.
- Parker JR. *Edge-Detection Techniques. Algorithms for Image Processing and Computer Vision*. 2nd ed. Indianapolis, IN: Wiley Publishers Inc; 2011:21–84.
- Harrison DA, Joos C, Ambrósio R Jr. Morphology of corneal basal epithelial cells by in vivo slit-scanning confocal microscopy. *Cornea*. 2003;22:246–248.
- Beucher S, Lantuejoul C. Use of watersheds in contour detection. Presented at: International Workshop on Image Processing, Real-time Edge and Motion Detection/Estimation; September 13–15, 1979; Rennes, France.
- Allgeier S, Zhivov A, Eberle F, et al. Image reconstruction of the subbasal nerve plexus with in vivo confocal microscopy. *Invest Ophthalmol Vis Sci*. 2011;52:5022–5028.
- Sindt CW, Lay B, Kern JR. ARIES: alconfocal rapid image evaluation system of corneal microstructure. *Invest Ophthalmol Vis Sci*. 2011;52:e-Abstract 1748.
- Niederer RL, Perumal D, Sherwin T, et al. Corneal innervation and cellular changes after corneal transplantation: an in vivo confocal microscopy study. *Invest Ophthalmol Vis Sci*. 2007;48:621–626.